

PAPER

View Article Online
View Journal | View IssueCite this: *J. Mater. Chem. A*, 2021, 9, 13151

Preparation of intergrown P/O-type biphasic layered oxides as high-performance cathodes for sodium ion batteries†

Kai Wang,^{ab cd} Zhen-Guo Wu,^{id ae} Georgian Melinte,^{* ch} Zu-Guang Yang,^a Abhishek Sarkar,^{id bc} Weibo Hua,^{id g} Xiaoke Mu,^c Zu-Wei Yin,^d Jun-Tao Li,^{id d} Xiao-Dong Guo,^{* a} Ben-He Zhong^a and Christian Kübel^{id * b c f h}

This study reports on the solid-state synthesis and characterization of novel quaternary P/O intergrown biphasic $\text{Na}_{0.8}\text{Mn}_y\text{Ni}_{0.8-y}\text{Fe}_{0.1}\text{Ti}_{0.1}\text{O}_2$ ($y = 0.6, 0.55, 0.5, 0.45$) cathode materials. Electrochemical tests reveal superior performance of the P/O biphasic materials in a sodium ion battery compared to the single P2 or O3 phases, proving the beneficial effect of the intergrowth of P2 and O3 materials. The nature of the P/O interface was studied by transmission electron microscopy. The analysis shows a semi-coherent interface grown along the a/b and c axes with local differences in the transition metal concentration along the interface between the two phases. EDX and EELS characterization revealed a charge compensation mechanism across the phase boundary based on variation of the transition element distribution, balancing the different sodium contents in the P and O phases. The results reported in this study provide a better understanding of P/O biphasic materials.

Received 22nd January 2021

Accepted 22nd April 2021

DOI: 10.1039/d1ta00627d

rsc.li/materials-a

Introduction

Electrochemical energy storage using renewable sources has significantly increased over the last few years, helping to reduce the excessive use of fossil fuels and the associated CO_2 emissions. Almost thirty years after the commercialization of lithium ion batteries (LIBs) for the first time,¹ LIBs have found extensive applications in many areas for a wide variety of products ranging from portable devices to electric vehicles and large energy storage facilities.^{2,3} However, the applications of LIBs, in particular for large-grid energy storage projects, are severely threatened by limited lithium reserves and the environment

problems associated with lithium mining and processing.⁴ As an alternative, sodium ion batteries (SIBs) have developed a strong competitive edge due to their electrochemical performance, which is starting to rival that of LIBs,⁵ and the almost inexhaustible sodium resources.^{6–8} However, the performance of their cathode materials still limits SIB performance.^{9,10} Cathode materials, including layered oxides,^{11–13} tunnel-structured oxides,^{14,15} phosphates,^{16,17} and sulfates,¹⁸ have been extensively researched. A promising system is the manganese-based layered oxide material, which exhibits high theoretical capacities, has low production costs and low environmental impact, and provides easy scale-up production capabilities.^{5–8}

In 1971, Parant *et al.* were the first to explore the sodium storage properties of layered Na_xMnO_2 ($x \leq 1$).¹⁹ Subsequently, manganese-based layered oxide materials were used as the first SIB prototypes due to their high capacity, low cost, and flexible production.²⁰ Two different kinds of Na^+ coordination configurations, P (prismatic) and O (octahedral), occur in layered oxides. Further considering the oxygen polyhedral stacking sequence, the materials have been identified as P2, O2, P3, and O3 (Fig. S1† shows the structure diagrams of P2 and O3 structures). Pure P and O phases exhibit distinct electrochemical properties, each with specific strengths and drawbacks. In particular, Mn-based P-type materials generally exhibit higher reversible capacities and better rate performances than O phase materials. However, insufficient sodium capacity severely limits the cathode performance and practical capacity of a full cell.²¹ Conversely, Mn-based O-type phases typically exhibit high

^aCollege of Chemical Engineering, Sichuan University, Chengdu 610065, China. E-mail: xiaodong2009@scu.edu.cn; zhenguowu@scu.edu.cn

^bDepartment of Materials and Earth Sciences, Technical University Darmstadt, Alarich-Weiss-Straße 2, 64287 Darmstadt, Germany

^cInstitute of Nanotechnology (INT), Karlsruhe Institute of Technology (KIT), Eggenstein-Leopoldshafen, D-76344, Germany. E-mail: christian.kuebel@kit.edu; georgian.melinte@kit.edu

^dCollege of Energy, Xiamen University, Xiamen 361005, China

^eCollege of Chemistry and Chemical Engineering, Xiamen University, Xiamen 361005, China

^fKarlsruhe Nano Micro Facility (KNMF), Karlsruhe Institute of Technology (KIT), Eggenstein-Leopoldshafen, D-76344, Germany

^gInstitute for Applied Materials, Karlsruhe Institute of Technology, Hermann-von-Helmholtz-Platz 1, 76344 Eggenstein-Leopoldshafen, Germany

^hHelmholtz Institute Ulm (HIU), Karlsruhe Institute of Technology (KIT), Helmholtzstraße 11, 89081 Ulm, Germany

† Electronic supplementary information (ESI) available. See DOI: 10.1039/d1ta00627d

coulombic efficiencies with high initial sodium contents. Nevertheless, the initial capacities and rate performances are inferior to P2 type materials due to the high Na^+ diffusion activation energy.²²

Many studies have focused on enhancing the electrochemical performances of layered oxide materials. These attempts can be categorized into two approaches.^{5,23–28} The first approach makes use of electrochemically inert transition metal (TM) ion doping that appears to be a good strategy to stabilize the structure of the layered oxide. During the sodiation–desodiation process, the valence states of the electrochemically active TM ions change in order to enable charge balance. However, Na^+ ions located near the inert TM sites are not removed from their prismatic/octahedral sites, and this has a stabilizing effect.²⁹ Ti, Cu, Mg, Zn, Li, and Mg are often chosen as doping elements in layered oxide SIB cathode materials due to their optimal ionic radii and low price.^{15,30–38} Yoshida *et al.* described a new P2-type $\text{Na}_{2/3}\text{Ni}_{1/3}\text{Mn}_{2/3-x}\text{Ti}_x\text{O}_2$ cathode material²⁶ and found that $\text{Na}_{2/3}\text{Ni}_{1/3}\text{Mn}_{1/2}\text{Ti}_{1/6}\text{O}_2$ delivers a high initial reversible capacity (127 mA h g^{-1}) and exhibits good capacity retention with a high average voltage of 3.7 V. Kang and coworkers showed that copper doping of a P2-type material ($\text{Na}_{0.67}\text{Cu}_x\text{Mn}_{1-x}\text{O}_2$), using a sol–gel method, can increase the average charge potential of the material and improve the cycling stability.³⁵ The $\text{Na}_{0.67}\text{Cu}_{0.25}\text{Mn}_{0.75}\text{O}_2$ sample retained more than 70% of the initial capacity after 500 cycles at 1000 mA g^{-1} and delivered an energy density of 260 W h kg^{-1} at a power density of 3000 W Kg^{-1} (calculated based on cathode mass). P2-Type $\text{Na}_x\text{Mg}_{0.11}\text{Mn}_{0.89}\text{O}_2$ also exhibited a very stable electrochemical performance, capable of delivering a high capacity retention of 93.8% after 100 cycles (compared to the 10th cycle).³⁸ An example for beneficial Zn doping was published by Wu *et al.*, who prepared P2-type $\text{Na}_{0.66}\text{Ni}_{0.33-x}\text{Zn}_x\text{Mn}_{0.67}\text{O}_2$ using a simple solid-state method, which exhibited a high capacity retention of 89% after 30 cycles due to Zn doping.³⁷

The second approach to improve the electrochemical properties of P and O type cathodes is to synthesize P/O-composites. Due to the structural and electrochemical differences of P- and O-type materials, some synergistic effects of the two phases appear in biphasic composites such as better structural stability during Na ion extraction and/or suppression of volume changes during cycling.^{5,39} These biphasic P/O cathodes show superior battery performance compared to single phase materials.^{27,28,34,40} Guo *et al.* reported on a P2/O3-type $\text{Na}_{0.66}\text{Li}_{0.18}\text{Mn}_{0.71}\text{Ni}_{0.21}\text{Co}_{0.08}\text{O}_{2+\sigma}$ composite, which showed excellent cycle performance with retention of 75% of the initial capacity after 150 cycles at 0.2C.²⁷ P/O-Type biphasic $\text{Na}_x\text{Mn}_y\text{Ni}_z\text{Fe}_{0.1}\text{Mg}_{0.1}\text{O}_2$ also showed a high capacity retention of 85.4% after 200 cycles at 0.1C.⁵ In particular, the extraordinary electrochemical performance of $\text{Na}_{0.76}\text{Mn}_{0.5}\text{Ni}_{0.3}\text{Fe}_{0.1}\text{Mg}_{0.1}\text{O}_2$ suggests that this material can be a major competitor to LiFePO_4 . However, the exact mechanism that leads to the superior battery properties of biphasic P/O materials is not fully understood. The coherence of the phase interface and the composition/state of the transition metals across the interface, especially, are still not clear.

In this work, we synthesized a novel P/O biphasic cathode for SIBs to combine the good battery performance of P/O

composites with the stabilizing effect of TM doping. Based on $\text{Na}_{2/3}\text{Mn}_{2/3}\text{Ni}_{1/3}\text{O}_2$, Fe and Ti with a concentration of 10% were selected as functional doping elements to design a series of $\text{Na}_x\text{Mn}_y\text{Ni}_z\text{Fe}_{0.1}\text{Ti}_{0.1}\text{O}_2$ materials. In order to better understand the internal structural information of the P/O biphasic material compared to its single-phase counterparts, analytical transmission electron microscopy (TEM) techniques capable of identifying the two nearly structurally identical P2 and O3 phases were employed to characterize the phases and their interfaces.

Experimental section

Material preparation

All P/O biphasic composites ($\text{Na}_{0.8}\text{Mn}_y\text{Ni}_{0.8-y}\text{Fe}_{0.1}\text{Ti}_{0.1}\text{O}_2$, $y = 0.6, 0.55, 0.5, 0.45$), P2-type $\text{Na}_{0.67}\text{Mn}_{0.55}\text{Ni}_{0.25}\text{Fe}_{0.1}\text{Ti}_{0.1}\text{O}_2$, and O3-type $\text{NaMn}_{0.55}\text{Ni}_{0.25}\text{Fe}_{0.1}\text{Ti}_{0.1}\text{O}_2$ materials in this study were prepared using a simple solid-state method. Stoichiometric ratios of Na_2CO_3 , Mn_2O_3 , NiO , Fe_2O_3 , and TiO_2 were mixed in a ball mill. The raw materials were ground for 2 h at 300 rpm using ethanol as a dispersant. The mixed materials were dried overnight in an oven at 100°C and pressed into approximately 5 mm thick pellets with a diameter of 20 mm. The pellets were calcined at 900°C for 15 h in a muffle oven with a heating rate of 5°C min^{-1} . After calcination, the pellets were slowly cooled to room temperature. The pellets were ground into fine powder and transferred into a glove box to avoid water and oxygen exposure until further use. The bulk chemical composition has been verified by ICP-OES (Table 1).

Material characterization

X-ray diffraction was conducted using a Rigaku D/Max-IV X-ray diffractometer with a $\text{Cu K}\alpha$ radiation source. The operating conditions were set as 40 kV and 30 mA. All XRD patterns were collected over a 2θ range of 10° – 80° at a scan rate of 2° min^{-1} . The Rietveld refinement of the XRD pattern was conducted using Topas V5.0 software (Topas V5, General profile and structure analysis software for powder diffraction data, Bruker AXS, Karlsruhe). The morphology of the powder samples was characterized by using a scanning electron microscope (SEM, Hitachi S-4800 SEM) equipped with an energy-dispersive X-ray spectrometer (EDS). A Titan 80-300 transmission electron microscope (FEI Company) operated at 300 kV and equipped with a CEOS image aberration corrector as well as with a US-1000 slow-scan CCD camera, a Tridien Gatan image filter (GIF) and a EDAX S-UTW EDS detector was used for detailed structural and elemental analysis.

Table 1 Overview of the ICP-OES results of the synthesized materials

Composition	Composition and ICP-OES results
$\text{Na}_{0.67}\text{Mn}_{0.55}\text{Ni}_{0.25}\text{Fe}_{0.1}\text{Ti}_{0.1}\text{O}_2$	$\text{Na}_{0.679}\text{Mn}_{0.564}\text{Ni}_{0.241}\text{Fe}_{0.102}\text{Ti}_{0.093}\text{O}_2$
$\text{Na}_{0.8}\text{Mn}_{0.55}\text{Ni}_{0.25}\text{Fe}_{0.1}\text{Ti}_{0.1}\text{O}_2$	$\text{Na}_{0.830}\text{Mn}_{0.554}\text{Ni}_{0.235}\text{Fe}_{0.116}\text{Ti}_{0.096}\text{O}_2$
$\text{NaMn}_{0.55}\text{Ni}_{0.25}\text{Fe}_{0.1}\text{Ti}_{0.1}\text{O}_2$	$\text{Na}_{1.002}\text{Mn}_{0.559}\text{Ni}_{0.241}\text{Fe}_{0.107}\text{Ti}_{0.093}\text{O}_2$



Electrochemical testing

The electrochemical performance of the materials was evaluated using CR2025 coin cells, which were assembled in a glove box. The glove box atmosphere was high-purity argon ($\geq 99.999\%$), and the oxygen and water partial pressures were maintained below 0.5 ppm. The cathode consisted of an active material, Super P, and polyvinylidene fluoride (PVDF) with a mass ratio of 8 : 1 : 1. The mass loading density of the active material was approximately 2.0 mg cm^{-2} . Glass fiber (GF/D Whatman) and pure sodium metal were used as the separator and anode, respectively. The electrolyte was $1.0 \text{ mol L}^{-1} \text{ NaClO}_4$ dissolved in ethylene carbonate (EC) and propylene carbonate (PC) with a volume ratio of 1 : 1. Galvanostatic charge and discharge tests were conducted within a voltage window of 1.5–4.3 V (vs. Na/Na^+) using a Land-CT2001A battery tester (Land Electronic Co., Ltd, Wuhan, China) at 30°C . In this study, a current density of 1C corresponds to 200 mA g^{-1} . Cyclic voltammetry (CV) was performed on a CHI660D electrochemical workstation (CH instruments Co., Ltd, Shanghai, China) using a scan rate of 0.2 mV s^{-1} between 1.5 and 4.3 V (vs. Na/Na^+).

Results and discussion

The Mn to Ni ratio of the $\text{Na}_{0.8}\text{Mn}_y\text{Ni}_{0.8-y}\text{Fe}_{0.1}\text{Ti}_{0.1}\text{O}_2$ was varied, with $y = 0.6, 0.55, 0.5, 0.45$. Fig. 1a shows the XRD patterns of the different samples, confirming the presence of both P2 and O3 phases. The reference Bragg diffraction peaks positions are shown at the bottom of the image. As shown in the enlarged XRD inset (angular range from 15° to 18°) in Fig. 1a, the XRD patterns of $\text{Na}_{0.8}\text{Mn}_y\text{Ni}_{0.8-y}\text{Fe}_{0.1}\text{Ti}_{0.1}\text{O}_2$ with $y = 0.55, 0.5, 0.45$ exhibit two peaks that can be assigned to the $\{002\}$ planes of the P2 phase (lower angle) and the $\{003\}$ planes of the O3 phase (higher angle), with the P2 : O3 peak intensity ratio decreasing with decreasing y . For $y = 0.6$, the material is a pure P2 phase. Other characteristic P2 and O3 peaks (e.g. at $\sim 32^\circ, 39^\circ, 41^\circ$, etc.) show a similar evolution, indicating that the O3 phase ratio increases with increasing Ni content. One can highlight that variations in the P2/O3 ratio in biphasic materials will also influence their electrochemical properties. Fig. 1b shows the cycle performances of the four materials. Although all three

mixed P/O phases show superior initial capacity compared to the single-phase sample, after 100 cycles the best discharge capacity retention is observed for $\text{Na}_{0.8}\text{Mn}_{0.55}\text{Ni}_{0.25}\text{Fe}_{0.1}\text{Ti}_{0.1}\text{O}_2$. Therefore, the $\text{Na}_{0.8}\text{Mn}_{0.55}\text{Ni}_{0.25}\text{Fe}_{0.1}\text{Ti}_{0.1}\text{O}_2$ material was further investigated in this study as the most promising biphasic material in this series.

Fig. 2 represents the refined XRD patterns of the single phase P2 and O3 materials, together with the selected biphasic composition, $\text{Na}_{0.8}\text{Mn}_{0.55}\text{Ni}_{0.25}\text{Fe}_{0.1}\text{Ti}_{0.1}\text{O}_2$. The diffraction pattern of the $\text{Na}_{0.67}\text{Mn}_{0.55}\text{Ni}_{0.25}\text{Fe}_{0.1}\text{Ti}_{0.1}\text{O}_2$ sample proves the presence of a pure P2 phase, which fits well with that of the standard P2 structure for the as-prepared material. For O3-type $\text{NaMn}_{0.55}\text{Ni}_{0.25}\text{Fe}_{0.1}\text{Ti}_{0.1}\text{O}_2$, there are small impurity peaks in the XRD pattern, which could be the result of some transition metal oxide impurities or other types of layered structures hard to identify uniquely due to their low reflection intensities. The XRD pattern of the biphasic material contains the peaks of both the P2 and O3 type phases, which belong to the $P6_3/mmc$ and $R\bar{3}mH$ space groups. The sharp peaks in the XRD pattern also indicate high crystallinity. The result of refinement demonstrates that the biphasic material matched the two phases well. The mass ratio of P2 : O3, determined from X-ray refinement, was found to be 73 : 27. In addition, Table 2 shows the detailed refinement data for the three materials. The values of R_p and the error χ^2 for the P2 and O3 materials from refinement are reasonable, suggesting that the refinement results are accurate. The details of Rietveld refinement including the atomic positions and possible occupancies are provided in the ESI.† SEM investigations of the morphology of particles are shown in Fig. 2d–f. The particles of all three materials consist of irregular plate-like shapes with sizes ranging from 0.5 to $4 \mu\text{m}$. Fig. S2† shows the particle size distributions of a 100 particles measured for each sample. The P2 material exhibits the largest particle size with most of the particles in the range of 0.5 to $2.5 \mu\text{m}$, while the O3-type material consists of particles with 0.5– $1.5 \mu\text{m}$ diameter. The particle size of the P/O biphasic material is between 0.5 and $2 \mu\text{m}$, in between that of the two pure phases.

X-ray diffraction has proved the coexistence of both P2 and O3 phases in $\text{Na}_{0.8}\text{Mn}_{0.55}\text{Ni}_{0.25}\text{Fe}_{0.1}\text{Ti}_{0.1}\text{O}_2$. In order to further demonstrate P/O phase intergrowth in single particles, high

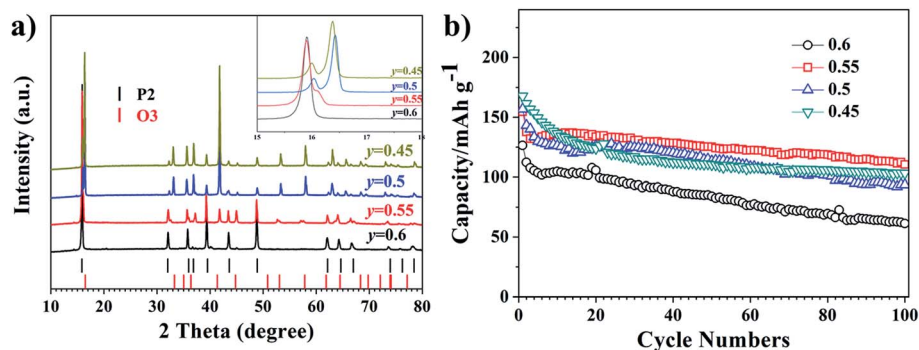


Fig. 1 (a) XRD patterns of $\text{Na}_{0.8}\text{Mn}_y\text{Ni}_{0.8-y}\text{Fe}_{0.1}\text{Ti}_{0.1}\text{O}_2$ ($y = 0.6, 0.55, 0.5, 0.45$) with the inset showing a magnified range (from 15° to 18°) corresponding to the (002) and (003) peaks of the P2 and O3 structures, respectively. (b) Cycling performance of $\text{Na}_{0.8}\text{Mn}_y\text{Ni}_{0.8-y}\text{Fe}_{0.1}\text{Ti}_{0.1}\text{O}_2$ ($y = 0.6, 0.55, 0.5, 0.45$).



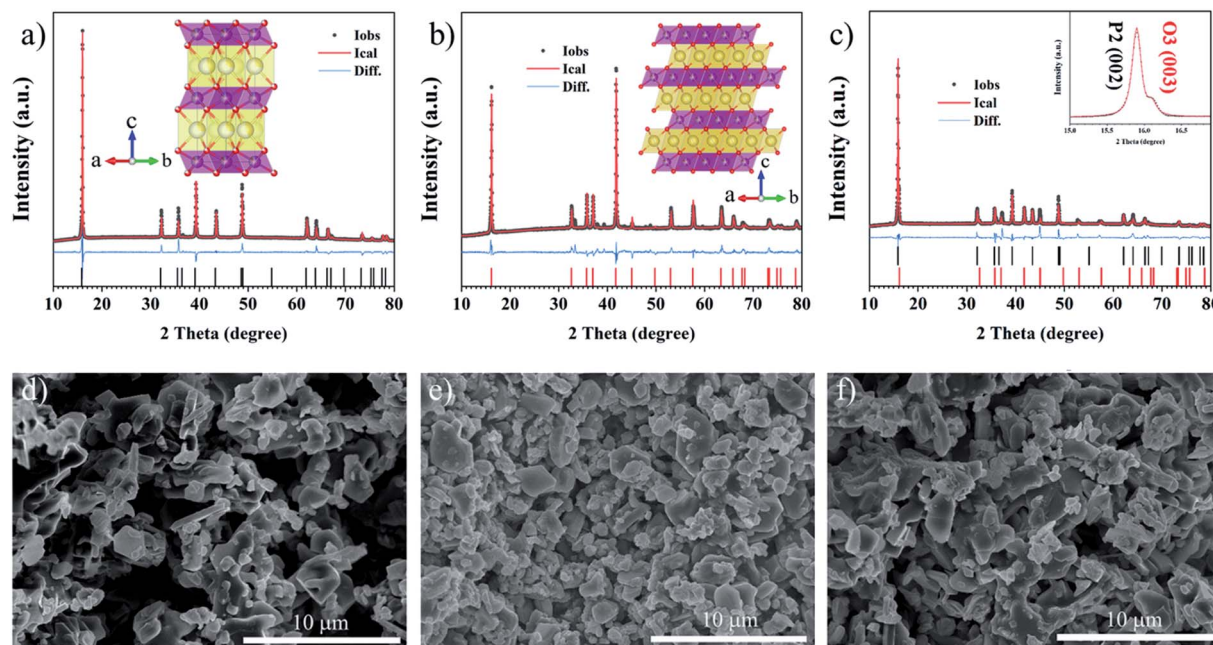


Fig. 2 XRD refinement and SEM images of the (a and d) P2, (b and e) O3, and (c and f) P/O biphasic materials. The structures in the inset are drawn using the Crystallographic Information File (cif) obtained after refinement of the experimental XRD patterns.

Table 2 Detailed crystallographic parameters and refinement errors for the three materials

	P2	O3	P/O biphasic	
Space group	$P6_3/mmc$	$R\bar{3}mH$	$P6_3/mmc$	$R\bar{3}mH$
$a = b/\text{\AA}$	2.9107(0)	2.9314(1)	2.90388(11)	2.9297(2)
$c/\text{\AA}$	11.1470(5)	16.4572(9)	11.1307(10)	16.487(2)
$V/\text{\AA}^3$	81.79(0)	122.47(1)	81.285(9)	122.55(2)
R_p (%)	2.07	2.57	3.14	
R_{wp} (%)	4.02	4.33	5.62	
GOF	3.81	3.70	5.36	
Mass ratio (%)			73.1(12)	26.9(12)

resolution TEM imaging and electron diffraction techniques were used. Due to the similarity of the crystal structure of the two phases, such as the space group and lattice parameters, it is impossible to distinguish P2 and O3 structures along the [001] direction. Due to the μm size plate-like morphology of the biphasic particles, with the [001] axis being shortest, TEM imaging along the a/b axis required cross-sectional sample preparation of the platelets. Therefore, focused ion beam (FIB) was used to prepare suitable samples for TEM characterization. Fig. 3a shows the morphology of the FIB prepared lamella with a thickness of 0.4λ (inelastic mean free path, Fig. S3†). The selected area electron diffraction (SAED) pattern from the region highlighted in Fig. 3a contains two different sets of diffraction spots, which can be indexed to the P2 and O3 structures, both viewed along the [110] direction (Fig. 3b). The high-resolution TEM image (Fig. 3c) allows us to clearly identify the interface between the two types of crystal lattices. Fast

Fourier transforms (FFT) of the two regions marked in Fig. 3c were chosen on each side of the P2/O3 interface and could be indexed as single P2 and O3 phases, respectively. The interface of the P2 and O3 structures was highlighted by inverse Fourier filtering of the initial high resolution image (Fig. 3f) with the selection of $(1\bar{1}1)/(112)$ spots of the O3 phase and $(111)/(110)$ spots of the P2 phase. The Fourier filtered image shows pure P2 and O3 structures grown together in a single particle around one well-defined interface. This finding is very important as powder XRD cannot distinguish an intergrown P2/O3 structure from a powder of single-phase mixed particles. Similar intergrown structures were also found by Xu *et al.* for P/O biphasic materials.²⁸ We believe that these intergrown particles are one reason for the excellent battery performance of biphasic materials, and this approach could be further studied in order to allow the design of new cathodes for SIBs. Although, P2 structures have high initial capacity, they always experience a partial irreversible transition to O2 during cycling due to structural distortions finally leading to collapse after Na ion removal. On the other hand, O3 phases show lower initial capacity but have better structural stability due to their closely packed structure. In intergrown biphasic particles, the O3 structure could improve the stability of the P2 structure by forming a stable interface with the O3 structure independent of the growth direction of the interface.⁵ An in-depth analysis of the P2/O3 interface was performed in order to understand the intergrowth geometry. The [110], [100] and [010] directions of the P2 crystal structure are symmetry equivalent (Fig. S4 top†). Similarly, the [100] and [010] directions in the O3 structure also exhibit identical projections (Fig. S4 bottom†). Therefore, the interfaces between P2 and O3 along the a - and b -axes are identical. Along the purple line marked by 'D' in Fig. 3f the



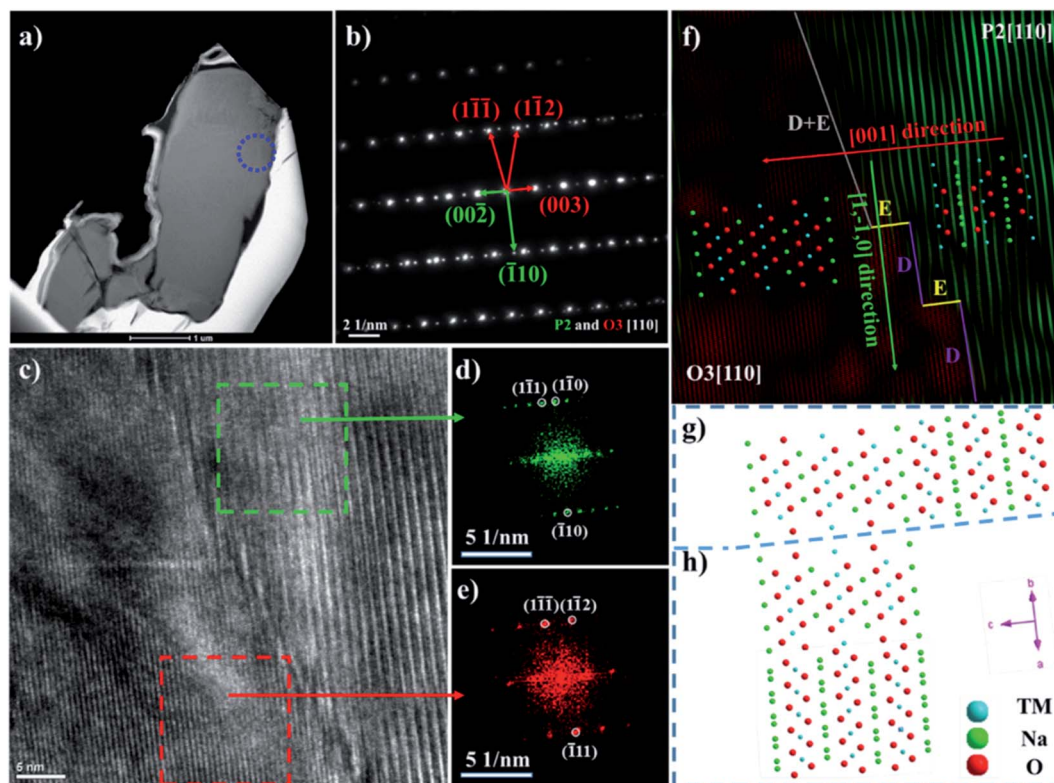


Fig. 3 S/TEM characterization of P/O biphasic $\text{Na}_{0.8}\text{Mn}_{0.55}\text{Ni}_{0.25}\text{Fe}_{0.1}\text{Ti}_{0.1}\text{O}_2$. (a) STEM image of the FIB prepared sample; (b) SAED from the area marked in (a); (c) HRTEM image of a P2/O3 interface in $\text{Na}_{0.8}\text{Mn}_{0.55}\text{Ni}_{0.25}\text{Fe}_{0.1}\text{Ti}_{0.1}\text{O}_2$ with (d) and (e) FFT from the areas marked in (c). (f) Inverse Fourier filtered HRTEM images of the P2 and O3 phases extracted from (c); (g) and (h) schematics of the two types of semi-coherent interfaces in the biphasic material.

interface is oriented along $[1\bar{1}0]$ with the $\{003\}$ facets of the O3 phase forming the interfacial plane (see schematic in Fig. 3g). The FFT analysis of the high-resolution TEM image around these regions (Fig. S5†) shows that the O3 $(1\bar{1}1)$ and P2 (111) reflections exhibit an angle of 3.7° . A 3.5% d -space difference between O3 $(1\bar{1}1)$ (2.56 Å) and P2 (111) (2.48 Å) could also be measured from the FFT. However, the very small 3.7° angle cannot compensate for the lattice difference between O3 $(1\bar{1}1)$ and P2 (111) found around the interface 'D'. Therefore, dislocations are present along the interface 'D' and the strain caused by these dislocations/distortions could enlarge the sodium diffusion path. The dislocations shown in Fig. S6† provide an indication for the structural effect of the strain introduced by dislocations along the boundary 'D'. In addition, an interface along the $[001]$ direction with the $\{100\}$ facets of O3 and P2 phases is present, forming a step-shape boundary structure along the yellow line marked as 'E' in Fig. 3f (schematic shown in Fig. 3g). The FFT analysis of the region around the 'E' interface (Fig. S5a†) shows that the P2 (002) and O3 (003) reflections are perfectly aligned. However, the lattice spacing of the P2 (002) and O3 (003) planes differs by about 1.5% (Fig. S5c†). This difference leads to a semi-coherent growth. Furthermore, the gray line labeled by 'D + E' indicates combined interface propagation consisting of small 'D' and 'E' type interface steps. In Fig. S7,† some longer interface examples of 'D' and 'E' types are shown in the enlarged image. The results

presented here indicate that the P2 and O3 structures intergrow in a single particle with a semi-coherent interface along both the a/b and the c -axes either as a smooth interface or with step-like propagation giving rise to more complex interface shapes. The semi-coherent interface is expected to be beneficial for sodium transition through the two phases as the inter-layer in the P2 and O3 phases is the main sodium-moving path, which is strained in P2 due to the interface. It could also suppress the collapse of the transition metal oxide layer in the P2 structure due to the stable O3 structure acting as template, thereby, making the biphasic material exhibit better cycle stability than the single P2 material.

The geometry of the Na^+ sites in the prismatic P2 and octahedral O3 phases leads to different amounts of Na^+ stabilized between the transition metal oxide layers. The O3 phase can maintain a higher Na^+ concentration compared to P2. However, the charge balance mechanism in an intergrown biphasic material composed of phases with different sodium contents is still not fully understood. STEM-EELS and EDX spectrum imaging was performed in order to assess the chemical properties of the intergrown P/O phases across their interface. Fig. 4a and b show the STEM-EDS maps of the constituting elements and their intensity profiles across the interface. As expected, the Na map shows a decrease in Na content in the P2 phase. A similar distribution difference is also observed for Fe and Ti. The intensity profiles shown in Fig. 4b reveal that the



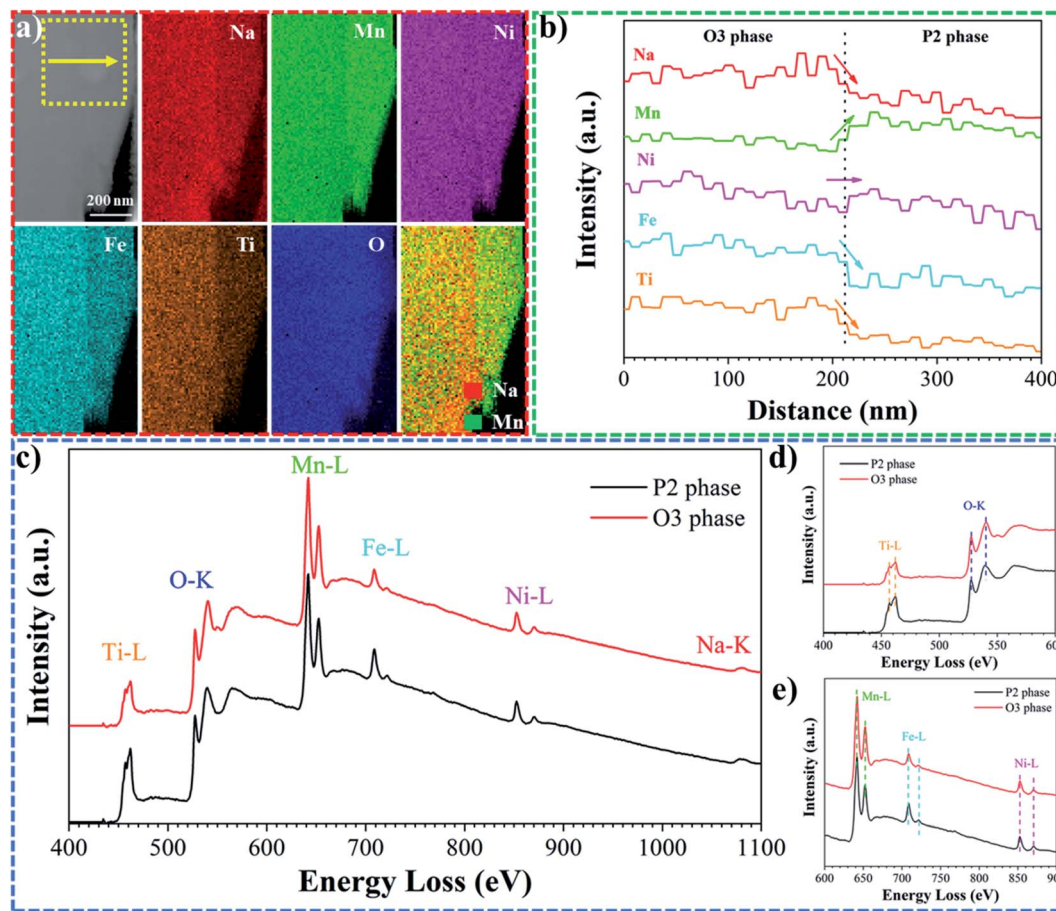


Fig. 4 a) STEM-EDX HAADF image and elemental distribution maps; (b) line profile representing the elemental intensities averaged over 360 nm parallel to the interface; (c) integrated EELS spectra from the P2 and O3 phases; (d) and (e) enlarged EELS spectra from (c) showing the edge position and shape to compare the oxidation state.

concentration of these elements exhibit a sharp drop at the O3/P2 interface. In contrast, the Mn map shows a sharp concentration increase in the P2 grain. The Ni and O maps (O is partially overlapped by the edges of transition metal L) show broader concentration variations without significant variations at the interface. Away from the interface, the composition of both the O3 and the P2 phases does not vary significantly. No changes can be observed in the line profile noticeably exceeding the standard deviation of the measurement of 2 to 5% (depending on the element). A STEM-EELS map across the P2/O3 interface (Fig. S8[†]) shows similar results. Fig. 4c shows two EELS spectra acquired from the P2 and O3 regions of the grain. It is well known that the L-edges of transition metals and the O K-edge are sensitive to their oxidation states. However, a closer look at the fine structure does not show a significant chemical shift, *i.e.* a change in position of the main edge, or variations of the L3/L2 peak ratio. This shows that in the biphasic particles, the charge balance due to the uneven Na distribution across the interface is not resolved by changes of the oxidation state of the constituent transition metals. Instead, the charge balance at the P2/O3 interface is achieved by varying the transition metal concentration during biphasic grain growth. This unexpected uneven distribution of TM ions along the interface might play

a positive role in the (semi)-coherent growth at the P2/O3 interface and the charge compensation mechanism during battery cycling. For instance, the interface could suppress the sliding of transition metal oxide layers in the P2 phase during the desodiation process due to the high stability of the O3 structure. The uniform oxidation state of the elements in both phases probably further supports the controlled, simultaneous sodium removal from both the P2 and O3 structures at the same voltage. Simultaneous sodium extraction from both phases would reduce the kinetic resistance.

The electrochemical behavior of the P-, the O-, and the P/O-type materials were tested using CV (Fig. 5). The CV of the P-type material presents two well-defined oxide peaks at around 2.4 and 3.7 V, corresponding to $\text{Mn}^{3+/4+}$ and $\text{Ni}^{2+/3+}$ transitions. Between the 1st and the 5th cycle, the intensity of the two redox peaks does not decrease significantly indicating a good initial reversibility. This unexpected stability of the P2 phase during the first cycles is mostly due to the overall stabilizing effect of both Fe and Ti metals.^{11,22} For the O3 phase, the $\text{Mn}^{3+/4+}$ oxide peak is shifted to higher voltage. In addition, the distance between the $\text{Mn}^{3+/4+}$ redox peaks is shifted to higher voltage compared to the P2 material corresponding to a higher energy density of the O3 material. The biphasic material shows an even



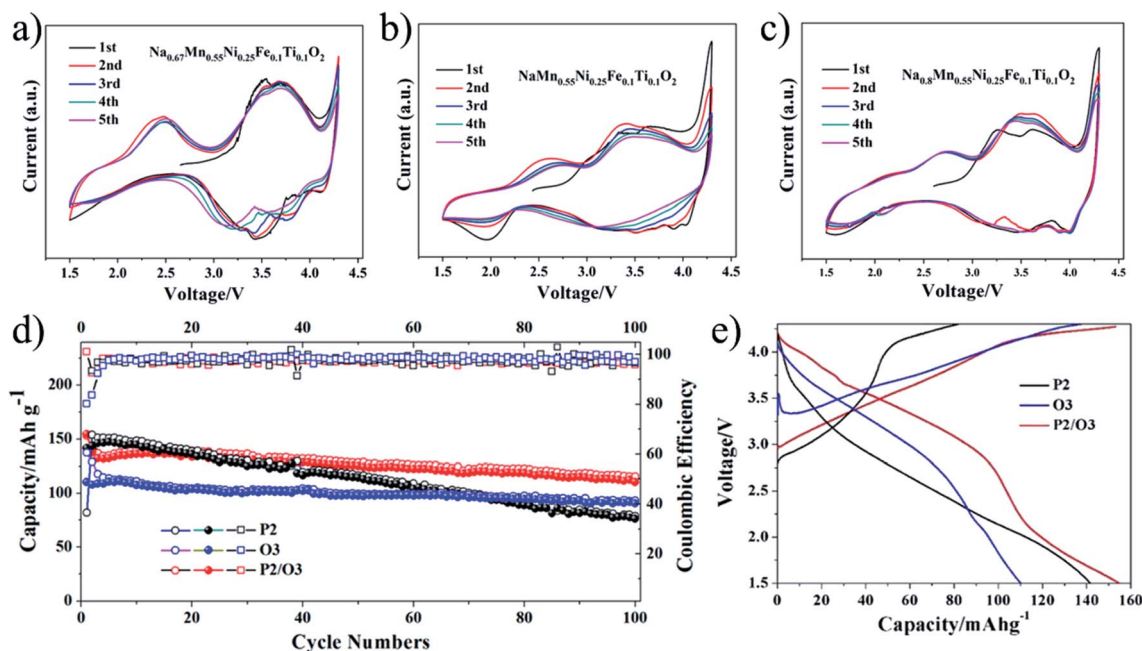


Fig. 5 The first five CV curves of the (a) P2-type, (b) O3-type, and (c) P/O biphasic-type materials; (d) cycling capacity of the three materials and (e) first cycle capacity–voltage curves of the three materials.

larger shift of the oxidation and reduction peaks towards a higher voltage (Fig. 5c), very smooth and broad peaks and good overlap of the curves after the 1st cycle. These properties are a clear indication of a solid solution reaction and higher energy density of the P/O biphasic material compared to the single-phase P2 material.

The electrochemical cycling performance of the as-prepared materials is shown in Fig. 5d. Overall, the P/O biphasic material exhibits the best cycling performance amongst the three samples. Although, the pure P2-type material has a higher initial capacity than the pure O3-type material, the inferior cycling stability results in poor capacity retention. Initially, a distinct decrease of the reversible capacity of the P/O biphasic material is detected. The slight capacity increase afterwards can be attributed to an activation process with electrolyte permeation.⁴¹ After 20 cycles, the biphasic material delivers higher capacity than the P2-type material due to its superior cycling stability. The pure O3-type material also exhibits a higher capacity than the P2-type material after the 76th cycle. After 100 cycles, the P/O intergrown $\text{Na}_{0.8}\text{Mn}_{0.55}\text{Ni}_{0.25}\text{Fe}_{0.1}\text{Ti}_{0.1}\text{O}_2$ structure exhibited a competitive capacity retention of 80.2% maintaining 110 mA h g^{-1} (compared to the 2nd cycle), which is much higher than for the pure P2-type material (about 53.8%). The discharge capacity of the O3 material after 100 cycles is not good (97 mA h g^{-1}) due to its low initial discharge capacity. The corresponding charge–discharge curves for the P-, O-, and P/O biphasic materials for the 1st, 2nd, 5th, 10th, 50th, and 100th cycles at 0.1C are shown in Fig. S10a–c.† Fig. S10d† depicts the energy density and average discharge voltage during long-term cycling, which show a similar trend to the cycling capacity. The voltage of the P/O biphasic material shows a noticeable decrease over the first few cycles as has been observed

previously *e.g.* by G.-L. Xu *et al.* and L. Eungje,^{28,42} which they related to structural changes affecting the sodium ion migration barrier that leads to different voltage profiles. The slight voltage increase following the initial decay has also been reported for some P/O biphasic materials^{39,43} in line with our observations. The P/O biphasic sample exhibited the highest energy density of 451 W h kg^{-1} due to the higher reversible capacity and voltage. Moreover, the P/O biphasic phase exhibited better rate performance than the P2- and O3-type materials as well (Fig. S10e†).

Fig. 5e shows the first charge–discharge curves of the as-prepared materials. The first charge capacity of the P2-type material is only 82 mA h g^{-1} , which is much lower than the corresponding discharge capacity of $\sim 142 \text{ mA h g}^{-1}$. As a result, the initial coulombic efficiency of the P2-type material is much higher than 100%, which makes anode coupling difficult and hinders practical applications.^{44,45} For the pure O3-type material, the first charge capacity of 138 mA h g^{-1} is higher than the respective discharge capacity of 110 mA h g^{-1} , which can be attributed to its sufficient sodium reservoir. However, the low initial coulombic efficiency of only $\sim 80\%$ limits the use of this phase as an active material in a full-cell. Unsurprisingly, the P/O-type material delivered the highest initial discharge capacity of around 153 mA h g^{-1} and an ideal initial coulombic efficiency of 101%. Moreover, the charge–discharge curves show that P/O biphasic $\text{Na}_{0.8}\text{Mn}_{0.55}\text{Ni}_{0.25}\text{Fe}_{0.1}\text{Ti}_{0.1}\text{O}_2$ exhibited higher discharge voltages with higher energy density than the pure phases.

Conclusion

In this study, a series of quaternary P/O biphasic materials was prepared by a simple solid-state method. A classical Mn-, Ni-



based sodium layer oxide cathode material system was chosen as the base system. 10% Fe and 10% Ti were introduced to improve the solid solution reaction during the charge and discharge processes and to enhance the cycling stability and energy efficiency. The atomic ratio of Mn and Ni was varied to determine the optimal ratio of Mn and Ni for the electrochemical performance and was set to $\text{Mn}_{0.55}$ and $\text{Ni}_{0.25}$. XRD and TEM results demonstrate that $\text{Na}_{0.8}\text{Mn}_{0.55}\text{Ni}_{0.25}\text{Fe}_{0.1}\text{Ti}_{0.1}\text{O}_2$ consists of both P2 and O3 phases. TEM characterization revealed that both phases can intergrow in a single particle with a semi-coherent interface along the *c* and *a*/*b* axes. Charge differences in the material caused by the different sodium contents of both phases are compensated by the different transition metal distribution on both sides of the interface. A superior reversible capacity of $154.6 \text{ mA h g}^{-1}$ with satisfying initial coulombic efficiency ($\sim 100\%$) of the biphasic material could be obtained together with an excellent capacity retention of 80.2% after 100 cycles at 0.1C. Moreover, the P/O biphasic material exhibited superior rate performance to and higher energy density than the pure P2 and O3 phases. The very good electrochemical performance of the biphasic material is attributed to the synergistic effects between the intergrown P2 and O3 phases enhancing both stability and ion mobility.

Author contributions

K. W. conceived the idea and discussed it with C. K., X. G., Z. W., G. M., X. M., Z. Y., J. L., and B. Z., and K. W. carried out the preparation experiments, electrochemical testing and TEM; Z. Y. performed the ICP-OES measurements; A. S. and W. H. performed the XRD refinements; the data were analysed by W. K. under the guidance of Z. W., G. M., C. K. and X. G.; the preliminary draft was written by K. W. with inputs from G. M. and C. K.; all authors contributed to reviewing and revising the manuscript.

Conflicts of interest

There are no conflicts of interest to declare.

Acknowledgements

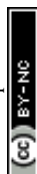
This work was supported by the National Natural Science Foundation of China (grant no. 21878195 and 21805198), Distinguished Young Scholars of Sichuan University (2017SCU04A08), Research Foundation for the Postdoctoral Program of Sichuan University (no. 2017SCU12018 and 2018SCU12045) and Karlsruhe Nano Micro Facility (KNMF). K. W. acknowledges financial support from the Chinese Scholarship Council (no. 201706240159). This work contributes to the research performed at CELEST (Center for Electrochemical Energy Storage Ulm-Karlsruhe) and was partially funded by the German Research Foundation (DFG) under Project ID 390874152 (POLiS Cluster of Excellence).

References

- 1 B. Scrosati, Lithium Rocking Chair Batteries: An Old Concept?, *J. Electrochem. Soc.*, 1992, **139**, 2776.
- 2 Y. Sun, Z. Wang, X. Huang and L. Chen, Synthesis and electrochemical performance of spinel $\text{LiMn}_{2-x-y}\text{Ni}_x\text{Cr}_y\text{O}_4$ as 5-V cathode materials for lithium ion batteries, *J. Power Sources*, 2004, **132**, 161–165.
- 3 A. R. Armstrong and P. G. Bruce, Synthesis of layered LiMnO_2 as an electrode for rechargeable lithium batteries, *Nature*, 1996, **381**, 499–500.
- 4 M. D. Slater, D. Kim, E. Lee and C. S. Johnson, Sodium-ion batteries, *Adv. Funct. Mater.*, 2013, **23**, 947–958.
- 5 M. Keller, D. Buchholz and S. Passerini, Correction to: Layered Na-Ion Cathodes with Outstanding Performance Resulting from the Synergetic Effect of Mixed P- and O-Type Phases, *Adv. Energy Mater.*, 2017, **7**, 1–11.
- 6 H. Pan, Y.-S. Hu and L. Chen, Room-temperature stationary sodium-ion batteries for large-scale electric energy storage, *Energy Environ. Sci.*, 2013, **6**, 2338.
- 7 S. P. Ong, V. L. Chevrier, G. Hautier, A. Jain, C. Moore, S. Kim, X. Ma and G. Ceder, Voltage, stability and diffusion barrier differences between sodium-ion and lithium-ion intercalation materials, *Energy Environ. Sci.*, 2011, **4**, 3680.
- 8 K. Wang, Z. G. Wu, T. Zhang, Y. P. Deng, J. T. Li, X. D. Guo, B. Bin Xu and B. H. Zhong, P2-type $\text{Na}_{0.67}\text{Mn}_{0.72}\text{Ni}_{0.14}\text{Co}_{0.14}\text{O}_2$ with K^+ doping as new high rate performance cathode material for sodium-ion batteries, *Electrochim. Acta*, 2016, **216**, 51–57.
- 9 V. Palomares, P. Serras, I. Villaluenga, K. B. Hueso, J. Carretero-González and T. Rojo, Na-ion batteries, recent advances and present challenges to become low cost energy storage systems, *Energy Environ. Sci.*, 2012, **5**, 5884.
- 10 W. F. Howard and R. M. Spotnitz, Theoretical evaluation of high-energy lithium metal phosphate cathode materials in Li-ion batteries, *J. Power Sources*, 2007, **165**, 887–891.
- 11 N. Yabuuchi, M. Kajiyama, J. Iwatate, H. Nishikawa, S. Hitomi, R. Okuyama, R. Usui, Y. Yamada and S. Komaba, P2-type $\text{Na}_x[\text{Fe}_{1/2}\text{Mn}_{1/2}]\text{O}_2$ made from earth-abundant elements for rechargeable Na batteries, *Nat. Mater.*, 2012, **11**, 512–517.
- 12 D. Kim, E. Lee, M. Slater, W. Lu, S. Rood and C. S. Johnson, Layered $\text{Na}[\text{Ni}_{1/3}\text{Fe}_{1/3}\text{Mn}_{1/3}]\text{O}_2$ cathodes for Na-ion battery application, *Electrochem. Commun.*, 2012, **18**, 66–69.
- 13 M. Sathiya, K. Hemalatha, K. Ramesha, J.-M. Tarascon and A. S. Prakash, Synthesis, Structure, and Electrochemical Properties of the Layered Sodium Insertion Cathode Material: $\text{NaNi}_{1/3}\text{Mn}_{1/3}\text{Co}_{1/3}\text{O}_2$, *Chem. Mater.*, 2012, **24**, 1846–1853.
- 14 P. Barpanda, G. Oyama, S. I. Nishimura, S. C. Chung and A. Yamada, A 3.8-V earth-abundant sodium battery electrode, *Nat. Commun.*, 2014, **5**, 1–8.
- 15 S. Guo, H. Yu, D. Liu, W. Tian, X. Liu, N. Hanada, M. Ishida and H. Zhou, A novel tunnel $\text{Na}_{0.61}\text{Ti}_{0.48}\text{Mn}_{0.52}\text{O}_2$ cathode material for sodium-ion batteries, *Chem. Commun.*, 2014, **50**, 7998.



- 16 M. Vujković and S. Mentus, Potentiodynamic and galvanostatic testing of $\text{NaFe}_{0.95}\text{V}_{0.05}\text{PO}_4/\text{C}$ composite in aqueous NaNO_3 solution, and the properties of aqueous $\text{Na}_{1.2}\text{V}_3\text{O}_8/\text{NaNO}_3/\text{NaFe}_{0.95}\text{V}_{0.05}\text{PO}_4/\text{C}$ battery, *J. Power Sources*, 2016, **325**, 185–193.
- 17 Y. Jiang, Z. Yang, W. Li, L. Zeng, F. Pan, M. Wang, X. Wei, G. Hu, L. Gu and Y. Yu, Nanoconfined carbon-coated $\text{Na}_3\text{V}_2(\text{PO}_4)_3$ particles in mesoporous carbon enabling ultralong cycle life for sodium-ion batteries, *Adv. Energy Mater.*, 2015, **5**, 1–8.
- 18 G. Oyama, S. ichi Nishimura, Y. Suzuki, M. Okubo and A. Yamada, Off-Stoichiometry in Alluaudite-Type Sodium Iron Sulfate $\text{Na}_{2+2x}\text{Fe}_{2-x}(\text{SO}_4)_3$ as an Advanced Sodium Battery Cathode Material, *ChemElectroChem*, 2015, **2**, 1019–1023.
- 19 J. P. Parant, R. Olazcuaga and M. Devalette, Sur quelques nouvelles phases de formule Na_xMnO_2 ($x \leq 1$), *J. Solid State*, 1971, **3**, 1–11.
- 20 N. Ortiz-vitoriano and N. E. Drewett, High performance manganese-based layered oxide cathodes: overcoming the challenges of sodium ion batteries, *Energy Environ. Sci.*, 2017, 1051–1074.
- 21 Z. Lu and J. R. Dahn, *In Situ* X-Ray Diffraction Study of $\text{P2-Na}_{2/3}[\text{Ni}_{1/3}\text{Mn}_{2/3}]\text{O}_2$, *J. Electrochem. Soc.*, 2001, **148**, A1225.
- 22 P. F. Wang, H. R. Yao, X. Y. Liu, J. N. Zhang, L. Gu, X. Q. Yu, Y. X. Yin and Y. G. Guo, Ti-Substituted $\text{NaNi}_{0.5}\text{Mn}_{0.5-x}\text{Ti}_x\text{O}_2$ Cathodes with Reversible O3–P3 Phase Transition for High-Performance Sodium-Ion Batteries, *Adv. Mater.*, 2017, **29**, 1–7.
- 23 S.-M. Oh, S.-T. Myung, J.-Y. Hwang, B. Scrosati, K. Amine and Y.-K. Sun, High Capacity O3-Type $\text{Na}[\text{Li}_{0.05}(\text{Ni}_{0.25}\text{Fe}_{0.25}\text{Mn}_{0.5})_{0.95}]\text{O}_2$ Cathode for Sodium Ion Batteries, *Chem. Mater.*, 2014, **26**, 6165–6171.
- 24 I. Hasa, D. Buchholz, S. Passerini, B. Scrosati and J. Hassoun, High Performance $\text{Na}_{0.5}[\text{Ni}_{0.23}\text{Fe}_{0.13}\text{Mn}_{0.63}]\text{O}_2$ Cathode for Sodium-Ion Batteries, *Adv. Energy Mater.*, 2014, **4**, 1400083.
- 25 R. Shanmugam and W. Lai, Study of Transport Properties and Interfacial Kinetics of $\text{Na}_{2/3}[\text{Ni}_{1/3}\text{Mn}_x\text{Ti}_{2/3-x}]\text{O}_2$ ($x = 0, 1/3$) as Electrodes for Na-Ion Batteries, *J. Electrochem. Soc.*, 2014, **162**, A8–A14.
- 26 H. Yoshida, N. Yabuuchi, K. Kubota, I. Ikeuchi, A. Garsuch, M. Schulz-Dobrick and S. Komaba, P2-type $\text{Na}_{2/3}\text{Ni}_{1/3}\text{Mn}_{2/3-x}\text{Ti}_x\text{O}_2$ as a new positive electrode for higher energy Na-ion batteries, *Chem. Commun.*, 2014, **50**, 3677–3680.
- 27 S. Guo, P. Liu, H. Yu, Y. Zhu, M. Chen, M. Ishida and H. Zhou, A layered P2- and O3-type composite as a high-energy cathode for rechargeable sodium-ion batteries, *Angew. Chem.*, 2015, **54**, 5894–5899.
- 28 G.-L. Xu, R. Amine, Y.-F. Xu, J. Liu, J. Gim, T. Ma, Y. Ren, C.-J. Sun, Y. Liu, X. Zhang, S. M. Heald, A. Solhy, I. Saadoune, W. L. Mattis, S.-G. Sun, Z. Chen and K. Amine, Insights into the structural effects of layered cathode materials for high voltage sodium-ion batteries, *Energy Environ. Sci.*, 2017, **10**, 1677–1693.
- 29 P.-F. Wang, Y. You, Y.-X. Yin, Y.-S. Wang, L.-J. Wan, L. Gu and Y.-G. Guo, Suppressing the P2-O2 Phase Transition of $\text{Na}_{0.67}\text{Mn}_{0.67}\text{Ni}_{0.33}\text{O}_2$ by Magnesium Substitution for Improved Sodium-Ion Batteries, *Angew. Chem.*, 2016, **128**, 7571–7575.
- 30 C. Zhang, R. Gao, L. Zheng, Y. Hao and X. Liu, New Insights into the Roles of Mg in Improving the Rate Capability and Cycling Stability of $\text{O3-NaMn}_{0.48}\text{Ni}_{0.2}\text{Fe}_{0.3}\text{Mg}_{0.02}\text{O}_2$ for Sodium-Ion Batteries, *ACS Appl. Mater. Interfaces*, 2018, **10**, 10819–10827.
- 31 H. Wang, Z. Li, W. Yang, J. Yang, D. Chen, C. Su and X. Liu, Structure modulation and performance optimization of Ni and Co for Fe, *Electrochim. Acta*, 2018, **277**, 88–99.
- 32 H. Wang, R. Gao, Z. Li, L. Sun, Z. Hu and X. Liu, Different Effects of Al Substitution for Mn or Fe on the Structure and Electrochemical Properties of $\text{Na}_{0.67}\text{Mn}_{0.5}\text{Fe}_{0.5}\text{O}_2$ as a Sodium Ion Battery Cathode Material, *Inorg. Chem.*, 2018, **57**, 5249–5257.
- 33 Z. Li, H. Wang, D. Chen, K. Sun, W. Yang and J. Yang, Improving the Performance of Layered Oxide Cathode Materials with Football-Like Hierarchical Structure for Na-Ion Batteries by Incorporating Mg^{2+} into Vacancies in Na-Ion Layers, *ChemSusChem*, 2018, **11**, 1223–1231.
- 34 Z. Y. Li, J. Zhang, R. Gao, H. Zhang, L. Zheng, Z. Hu and X. Liu, Li-substituted Co-free layered P2/O3 biphasic $\text{Na}_{0.67}\text{Mn}_{0.55}\text{Ni}_{0.25}\text{Ti}_{0.2-x}\text{Li}_x\text{O}_2$ as high-rate-capability cathode materials for sodium ion batteries, *J. Phys. Chem. C*, 2016, **120**, 9007–9016.
- 35 W. Kang, Z. Zhang, P.-K. Lee, T.-W. Ng, W. Li, Y. Tang, W. Zhang, C.-S. Lee and D. Y. Wai Yu, Copper substituted P2-type $\text{Na}_{0.67}\text{Cu}_x\text{Mn}_{1-x}\text{O}_2$: a stable high-power sodium-ion battery cathode, *J. Mater. Chem. A*, 2015, **3**, 22846–22852.
- 36 M. Choi, I. H. Jo, S. H. Lee, Y. Il Jung, J. K. Moon and W. K. Choi, A facile synthesis and electrochemical performance of $\text{Na}_{0.6}\text{Li}_{0.6}[\text{Mn}_{0.72}\text{Ni}_{0.18}\text{Co}_{0.10}]\text{O}_2$ as cathode materials for Li and Na ion batteries, *Curr. Appl. Phys.*, 2016, **16**, 226–230.
- 37 X. Wu, J. Guo, D. Wang, G. Zhong, M. J. McDonald and Y. Yang, P2-type $\text{Na}_{0.66}\text{Ni}_{0.33-x}\text{Zn}_x\text{Mn}_{0.67}\text{O}_2$ as new high-voltage cathode materials for sodium-ion batteries, *J. Power Sources*, 2015, **281**, 18–26.
- 38 D. Buchholz, C. Vaalma, L. G. Chagas and S. Passerini, Mg-Doping for improved long-term cyclability of layered Na-ion cathode materials - The example of P2-type $\text{Na}_x\text{Mg}_{0.11}\text{Mn}_{0.89}\text{O}_2$, *J. Power Sources*, 2015, **282**, 581–585.
- 39 J. Chen, L. Li, L. Wu and Q. Yao, Enhanced cycle stability of $\text{Na}_{0.9}\text{Ni}_{0.45}\text{Mn}_{0.55}\text{O}_2$ through tailoring O3/P2 hybrid structures for sodium-ion batteries, *J. Power Sources*, 2018, **406**, 110–117.
- 40 M. Bianchini, E. Gonzalo, N. Drewett, N. Ortiz Vitoriano, J.-M. Lopez del Amo, F. J. Bonilla, B. Acebedo and T. Rojo, Layered P2–O3 sodium-ion cathodes derived from earth abundant elements, *J. Mater. Chem. A*, 2018, **6**, 3552.
- 41 S. Doubaji, M. Valvo, I. Saadoune, M. Dahbi and K. Edström, Synthesis and characterization of a new layered cathode material for sodium ion batteries, *J. Power Sources*, 2014, **266**, 275–281.



- 42 E. Lee, J. Lu, Y. Ren and X. Luo, Layered P2/O3 Intergrowth Cathode: Toward High Power Na-Ion Batteries, *Adv. Energy Mater.*, 2014, **4**, 1400458.
- 43 B. Hu, F. Geng, C. Zhao, B. Doumert, J. Trébosc, O. Lafon and C. Li, Deciphering the Origin of High Electrochemical Performance in a Novel Ti-Substituted P2/O3 Biphasic Cathode for Sodium-Ion Batteries, *ACS Appl. Mater. Interfaces*, 2020, **12**, 41485–41494.
- 44 G. Singh, B. Acebedo, M. C. Cabanas, D. Shanmukaraj, M. Armand and T. Rojo, An approach to overcome first cycle irreversible capacity in P2-Na_{2/3}[Fe_{1/2}Mn_{1/2}]O₂, *Electrochem. Commun.*, 2013, **37**, 61–63.
- 45 J. Martinez De Ilarduya, L. Otaegui, J. M. López del Amo, M. Armand and G. Singh, NaN₃ addition, a strategy to overcome the problem of sodium deficiency in P2-Na_{0.67}[Fe_{0.5}Mn_{0.5}]O₂ cathode for sodium-ion battery, *J. Power Sources*, 2017, **337**, 197–203.

